Article submitted to: High Power Laser Science and Engineering, 2026 *September 16, 2026*

A Novel Backpropagation-Based Method for Assembly Preload Optimization in Stress-Induced Polarization Smoothing

Honghong Wu[1], Yu Xie[2], Xibo Sun[2,*], Qiang Yuan[2], Hui Wang[3,*], Yuting Wu[4], Yilin Yao[2], Han Gu[2], Huan Pang[2], Qier An[2], Xuanyi Da[2], and Zunmin Geng[1]

[1]*School of Mechanical Engineering and Automation, Beihang University, Beijing 102206, China*
[2]*Research Center of Laser Fusion, China Academy of Engineering Physics, Mianyang 621900, China*
[3]*Research Institute of Aero-Engine, Beihang University, Beijing 102206, China*
[4]*Laboratory of Robotics and Systems, Harbin Institute of Technology, Harbin 150080, China*

Abstract

This study proposes an assembly-preload optimization method for polarization smoothing in high-power laser facilities using stress-induced birefringence in a fused silica vacuum window. A discrete opto-mechanical model is developed by coupling force–optics interactions with the window boundary constraints and assembly configuration. Based on this model, a backpropagation-based framework optimizes preload magnitude, loading position, and contact stiffness via gradient descent, with focal-spot irradiation uniformity as the objective. Under optimized conditions, 29% of the incident P-polarized light is converted to S polarization at 532 nm, increasing to 41% at the design wavelength of 351 nm, while the Precision Diagnostic System verified a relative RMS contrast of approximately 0.77 at 351 nm, with high-intensity speckles significantly suppressed and no noticeable wavefront distortion or near-field modulation. The proposed method improves irradiation uniformity while preserving beam quality, providing a practical strategy for preload optimization in polarization smoothing.

Keywords: Polarization smoothing; Mechanical stress-induced birefringence; Opto-mechanical analysis; Preload optimization

1. Introduction

Laser inertial confinement fusion (ICF) relies on high-power laser pulses to drive the implosion of deuterium–tritium (DT) fuel capsules, with the ultimate goal of achieving fusion ignition and high energy gain[1,2]. During this process, laser–plasma instabilities (LPIs), including stimulated Raman scattering (SRS) and stimulated Brillouin scattering (SBS), will degrade laser energy coupling and induce drive asymmetries, thereby posing significant challenges to achieving fusion ignition[3–6]. The growth of LPIs is strongly correlated with increasing laser intensity and irradiation nonuniformity. Consequently, with the continuous enhancement of the output capability of high-power ICF laser drivers, active manipulation of laser irradiation uniformity has become essential for suppressing the growth of LPIs and improving implosion performance[7,8]. Representative large-aperture high-power laser drivers, including the National Ignition Facility (NIF) in the United States, the Laser Mégajoule (LMJ) facility in France, and the 100-kJ laser facility in China, have incorporated beam smoothing techniques as indispensable components for controlling focal spot distributions and improving laser–target coupling efficiency[9–12]. These approaches are generally categorized into spatial smoothing, temporal smoothing, and polarization smoothing[13–15].

Spatial smoothing techniques, represented by the random phase plate (RPP) proposed by Kato et al. and the continuous phase plate (CPP) developed by Dixit et al., modulate the wavefront distribution of the large-aperture laser beam to generate a focal spot with a smooth intensity envelope on the target plane, thereby improving the spatial uniformity of the focal spot distribution[16,17]. However, the phase modulation inevitably results in small-scale speckle structures

Correspondence to: *Hui Wang, Research Institute of Aero-Engine, Beihang University, Beijing 102206, China. Email: wanghuisx@gmail.com; *Xibo Sun, Research Center of Laser Fusion, China Academy of Engineering Physics, Mianyang 621900, China. Email: sxb_09@163.com

This peer-reviewed article has been accepted for publication but not yet copyedited or typeset, and so may be subject to change during the production process. The article is considered published and may be cited using its DOI.
This is an Open Access article, distributed under the terms of the Creative Commons Attribution licence (https://creativecommons.org/licenses/by/4.0/), which permits unrestricted re-use, distribution, and reproduction in any medium, provided the original work is properly cited.
10.1017/hpl.2026.10224

Downloaded from https://www.cambridge.org/core. 11 Nov 2026 at 09:59:05, subject to the Cambridge Core terms of use.

in the far field due to coherent interference, accompanied by high-contrast and high-spatial-frequency intensity modulations. Although advanced optimization methods, such as improved Gerchberg–Saxton (G–S) algorithms, have been developed in recent years to refine the phase distribution of phase plates, these high-energy small-scale speckles remain difficult to eliminate[18,19]. Excessive high-spatial-frequency components may induce surface perturbations on the fuel capsule, providing initial seeds for Rayleigh–Taylor (RT) instabilities and further enhancing the growth of LPIs[20,21]. Temporal smoothing techniques are designed to suppress these high-spatial-frequency speckle components through temporal averaging or decorrelation. Induced spatial incoherence (ISI), proposed by Lehmberg et al., introduces optical path delays exceeding the laser coherence time across the beam aperture, causing the interference pattern to rapidly evolve with time[22,23]. Smoothing by spectral dispersion (SSD), proposed by Skupsky et al., employs electro-optic phase modulation and diffraction gratings to generate spatially dependent frequency shifts across the laser beam, thereby reducing speckle contrast through temporal integration[24]. Although temporal smoothing techniques are highly effective in suppressing medium- and high-spatial-frequency nonuniformities, their smoothing performance is inherently constrained by the finite duration of laser pulses and the available time for intensity averaging.

Polarization smoothing (PS) techniques reduce focal spot intensity contrast by exploiting the incoherent superposition of orthogonally polarized beams. Rothenberg demonstrated that, when interference between orthogonal polarization components is eliminated, PS can instantaneously reduce RMS nonuniformity of the focal spot to $1/\sqrt{2}$ of its initial value, independent of the laser pulse duration[25]. Michel further clarified the underlying physical mechanisms linking PS to LPI suppression[26]. More importantly, polarization diversity on the target plane can effectively disrupt the phase-matching conditions required for parametric instabilities, such as SRS and SBS, which is essential for suppressing rapidly growing LPIs[27]. Current PS schemes employed in ICF laser drivers can be generally classified into two categories: inter-beam polarization smoothing and intra-beam polarization smoothing. Inter-beam PS adjusts the polarization states of individual sub-beams within the beamlet by arranging wave plates in their respective optical paths, thereby enabling incoherent superposition among these sub-beams[28,29]. In contrast, intra-beam PS directly introduces polarization diversity into the originally linearly polarized third-harmonic (3ω, 351 nm) beam[30]. The representative approach utilizes the birefringence properties of large-aperture KDP/DKDP crystals to convert the incident laser beam into two spatially separated orthogonal polarization components[31–34]. The intra-beam PS enables more effective suppression of high-intensity speckle fractions on the target plane. However, The KDP-based crystal optics experience transverse stimulated Raman scattering (TSRS) under ultraviolet laser irradiation[35,36]. The TSRS gain increases exponentially along the transverse direction of the crystal aperture, which significantly restricts the operational safety margin of this approach in high-energy ultraviolet laser systems.

Stress-induced birefringence can provide a new pathway for achieving polarization smoothing using isotropic materials. Within the elastic regime, the linear and controllable mechanical response to the applied load provides a feasible basis for active optical polarization control. By exploiting mechanically induced birefringence, polarization smoothing can be actively implemented in materials with higher laser damage thresholds, such as fused silica. Spilman et al. realized a stress-induced spatially varying waveplate in the circular BK7 window using three-point symmetric mechanical preloading[37,38]. This approach locally converted linearly polarized light into vector vortex beams, thereby demonstrating the feasibility of active polarization control through mechanical stress. Liu et al. subsequently investigated the stress-induced birefringence in small-aperture optical plates through numerical simulations, providing valuable insights into the analysis of optical responses arising from assembly-induced stresses in optics[39]. However, existing studies on mechanical stress-induced birefringence for polarization control have largely been limited to simple polarization manipulation in small-aperture optics or have primarily focused on suppressing parasitic birefringence induced by assembly stresses. Extending stress-induced birefringence to polarization smoothing of large-aperture laser beams in ICF laser drivers still faces several fundamental challenges. First, stress-induced polarization smoothing of large-aperture laser beams on the target plane relies on the coordinated interaction of multiple coupled physical fields, making the inverse determination of the required stress field from the desired physical response highly challenging. Second, the relationship between the applied preload and the internal stress field during assembly is governed by complex boundary constraints and stress transmission paths, rendering conventional empirical design approaches inadequate. Finally, stress-induced polarization modulation must avoid excessive wavefront distortion and near-field modulation to ensure the beam quality required for ICF laser drivers.

As the core algorithm of differentiable programming, the backpropagation (BP) algorithm leverages the chain rule to efficiently compute the gradients of input parameters from output errors, making it a powerful tool for goal-oriented inverse design[40]. To date, this approach has been successfully applied to the optimization of high-power optical systems, including the phase distribution design of CPPs[41]. To address the aforementioned challenges, this study introduces a BP-based framework and proposes the active mechanical loading strategy for stress-induced polarization smoothing. First, the coupling mechanism between the applied preload

Downloaded from https://www.cambridge.org/core. 11 Nov 2026 at 09:59:05, subject to the Cambridge Core terms of use.

and the internal stress tensor is elucidated, and a parametric mapping model linking preload parameters, edge pressure, and the internal stress field is established. Second, an opto-mechanical coupling model incorporating assembly parameters is developed to quantitatively reveal the influence of the stress field on polarization states and focal spot energy distributions. Finally, the preload parameters are iteratively optimized through the BP framework, enabling high-precision active control of irradiation uniformity on the target plane.

2. Material and Methodology

2.1. Optical Functional Carrier

The isotropic fused silica serves as a critical material in high-power laser facilities, primarily due to its outstanding optical transparency, excellent resistance to optical damage, and remarkable growth uniformity. It is widely utilized in key optical components, such as shielding plates, reflectors, wedged lenses (WFL), and vacuum windows (VW). Positioned between the target chamber and the final optics assembly, the VW serves to isolate the air connection between them, maintaining an ultra-high vacuum (UHV) environment of approximately 10^{-4} to 10^{-3} Pa within the target chamber. Consequently, the VW must withstand substantial differential pressure. The mechanical parameters of fused silica are summarized in Table 1. Notably, the peak compressive strength reaches 1.14 GPa, which is sufficient to withstand most high-magnitude pressures without stress concentration. Furthermore, the high elastic modulus coupled with a low Poisson's ratio ensures that deformations under tensile or compressive loads remain micro-scale within the elastic regime. Consequently, the impact on surface figure degradation is minimal, which is highly advantageous for mechanical clamping aimed at acquiring the stress tensor field.

Table 1. Mechanical properties of the fused silica (Corning 7980).

Mechanical property	Value
Young's modulus (E)	73 GPa
Fracture modulus after abrasion	52.4 GPa
Bulk modulus (K)	35.9 GPa
Poisson's ratio (ν)	0.16
Density (ρ)	2.20 g/cm^3
Knoop hardness (100 g load)	522 kg/mm^2
Tensile strength	54 MPa
Compressive strength	1.14 GPa

As an isotropic and linearly elastic photoelastic medium, fused silica exhibits microscopic anisotropy when deformed within the elastic regime under external loading. The stress-optic coupling effect is quantitatively described using the refractive index ellipsoid formalism:

Table 2. Optical parameters of the fused silica (Corning 7980).

Optical parameter	Value
Refractive index n_0 at 351 nm	1.4764
Piezo-optic coefficient π_{11}	0.4279 TPa^{-1}
Piezo-optic coefficient π_{12}	2.8107 TPa^{-1}
Piezo-optic coefficient π_{44}	$\pi_{11} - \pi_{12}$

$$\sum_{i,j} B_{ij} x_i x_j = 1, \quad \text{where } i, j = 1, 2, 3 \tag{1}$$

In Eq. (1), x_i $(i = 1, 2, 3)$ denote the Cartesian coordinates corresponding to the x, y, and z axes, respectively; B_{ij} $(i, j = 1, 2, 3)$ represent the components of the dielectric impermeability tensor $\boldsymbol{B}$. For isotropic fused silica, the dielectric impermeability tensor is expressed in matrix form as:

$$\boldsymbol{B} = \begin{bmatrix} B_{11} & B_{12} & B_{13} \\ B_{21} & B_{22} & B_{23} \\ B_{31} & B_{32} & B_{33} \end{bmatrix}, \quad \text{where } B_{ij} = B_{ji} \tag{2}$$

Under the initial condition without external loading or any inhomogeneity, the tensor components in Eq. (2) satisfy $B_{11} = B_{22} = B_{33} = 1/n_0^2$ and $B_{12} = B_{23} = B_{13} = 0$, where n_0 is the refractive index in the unstressed state. Under external loading, referring to the Cartesian coordinate system in which the stress vector $\boldsymbol{\sigma} = [\sigma_x,\ \sigma_y,\ \sigma_z,\ \tau_{xy},\ \tau_{yz},\ \tau_{zx}]^{\mathrm{T}}$ is defined, the impermeability tensor $\boldsymbol{B} = [B_{11},\ B_{22},\ B_{33},\ B_{12},\ B_{23},\ B_{13}]^{\mathrm{T}}$ are linearly related to the stress components as follows:

$$\boldsymbol{B} = \boldsymbol{B}^0 + \boldsymbol{\pi} \cdot \boldsymbol{\sigma} \tag{3}$$

$$\boldsymbol{\pi} = \begin{bmatrix} \pi_{11} & \pi_{12} & \pi_{12} & 0 & 0 & 0 \\ \pi_{12} & \pi_{11} & \pi_{12} & 0 & 0 & 0 \\ \pi_{12} & \pi_{12} & \pi_{11} & 0 & 0 & 0 \\ 0 & 0 & 0 & \pi_{44} & 0 & 0 \\ 0 & 0 & 0 & 0 & \pi_{44} & 0 \\ 0 & 0 & 0 & 0 & 0 & \pi_{44} \end{bmatrix} \tag{4}$$

Here, $\boldsymbol{\pi}$ denotes the piezo-optic coefficient matrix. The numerical values of $\boldsymbol{\pi}$ for fused silica glass are summarized in Table 2.

For an arbitrary propagation direction, the optical properties of the medium are governed by the elliptical cross-section of the refractive index ellipsoid normal to that direction. For the large-aperture fused silica optics, the beam propagation direction is perpendicular to the entrance surface of the element. By defining the x-y plane as the entrance surface (with the length and width aligned along the x- and y-axes, respectively), the beam propagation direction coincides with the z-axis of the Cartesian coordinate system. In this

Downloaded from https://www.cambridge.org/core. 11 Nov 2026 at 09:59:05, subject to the Cambridge Core terms of use.

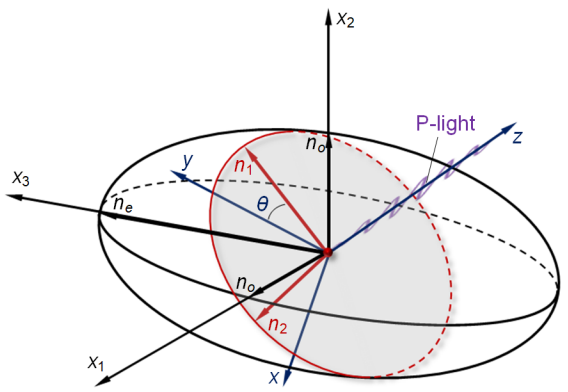


Figure 1. Variation of refractive index parameters under external stress. In an isotropic medium, mechanical stress distorts the refractive index surface from a perfect sphere into an ellipsoid, leading to $n_e \neq n_o$. The effective refractive index for light propagation is determined by the elliptical cross-section of the refractive index ellipsoid normal to the wave vector. The inset schematically illustrates the stress-induced birefringence parameters and the corresponding elliptical cross-section for light propagating along the z-axis.

configuration, the stress-induced birefringence experienced by the beam is governed by the elliptical cross-section of the refractive index ellipsoid in the x-y plane, as illustrated in Figs. 1 and 2(a). Analytical solution of the elliptical cross-section yields the principal polarization parameters governing beam propagation, namely the slow-axis refractive index n_1, the fast-axis refractive index n_2, and the optic-axis azimuth θ (which is defined as the rotation angle of the major axis about the z-axis):

$$\theta = \begin{cases} \theta' & , \quad B_{11} > B_{22} \\ \theta' + \pi/2 & , \quad B_{11} < B_{22},\ \theta' < 0 \\ \theta' - \pi/2 & , \quad B_{11} < B_{22},\ \theta' > 0 \end{cases} \tag{5}$$

where $\theta' = \frac{1}{2}\tan^{-1}\left(\frac{2B_{12}}{B_{11}-B_{22}}\right)$.

$$n_{1,2}^2 = \frac{2}{(B_{11}+B_{22}) \mp \sqrt{4B_{12}^2 + (B_{11}-B_{22})^2}} \tag{6}$$

According to Eqs. (3)–(6), for the z-directed beam propagation, the refractive index n_1 and n_2 depend exclusively on the dielectric impermeability tensor elements B_{11}, B_{12}, and B_{22}, which are functions of the stress components σ_x, σ_y, and τ_{xy}. Evidently, the normal stresses σ_x and σ_y, acting along the x- and y-directions respectively, together with the shear stress τ_{xy} in the x–y plane, constitute a plane stress state confined to the x–y plane. This implies that any attempt to modify the stress-induced birefringence of an optical element via stress vectors must rely on the relative magnitudes and spatial distributions of these plane stress components as the primary evaluation metrics.

In the birefringent medium, the difference in refractive indices between the fast and slow axes leads to different phase velocities for orthogonally polarized waves. After traversing the same physical path length, the two polarization components acquire a relative phase retardation δ:

$$\delta = \varphi_1 - \varphi_2 = \frac{2\pi}{\lambda}\int_0^d (n_1(z) - n_2(z))\, dz \tag{7}$$

where φ_1 and φ_2 denote the phases of the optical waves polarized along the slow and fast axes, respectively, and d is the propagation distance through the medium.

As indicated by Eqs. (6) and (7), both the magnitudes of the stress components and the integrated thickness of the optical element contribute positively to the accumulated phase retardation δ.

Moreover, for large-aperture optical elements employed in high-power laser systems, a relatively small thickness (e.g., shielding plates of 430 mm×430 mm×10 mm) combined with high clamping loads tends to increase the risk of mechanical instability and damage. In contrast, the larger thickness of the VW provides higher bending stiffness and a greater mechanical safety margin under lateral loading. Taking these factors into account, the VW represents a more appropriate choice for implementing stress-induced birefringence as a polarization smoothing mechanism.

As shown in Figs. 2(a) and 2(b), the VW employed in the high-power laser system has dimensions of 430 mm × 430 mm × 43 mm, yielding a width-to-thickness ratio in the range of 8–10, which satisfies the condition for the plane stress assumption. This implies that when a mechanical load is applied to the side faces of the window, the resulting stress field is essentially a plane stress state confined to the x–y plane. Moreover, lateral loading minimizes the impact on the clear aperture while still generating the required stress distribution.

2.2. *Coupled Stress–Boundary Response Analysis*

2.2.1. *Mechanical Model*

Given that the stress-induced deformation is negligible relative to the overall dimensions of the VW, and that the resulting strain remains within the elastic limit, the mechanical response of the optic can be modeled using linear elasticity theory. The displacement field is given by $\boldsymbol{u} = u\,\boldsymbol{e}_x + v\,\boldsymbol{e}_y + w\,\boldsymbol{e}_z$, where (u, v, w) are the displacement components in the Cartesian system. The stress-induced strain tensor $\boldsymbol{\varepsilon} = [\varepsilon_x,\ \varepsilon_y,\ \varepsilon_z,\ \gamma_{xy},\ \gamma_{yz},\ \gamma_{zx}]^{\mathrm{T}}$ can be related to the nodal displacements as follows:

$$\varepsilon = \left[\frac{\partial u}{\partial x},\ \frac{\partial v}{\partial y},\ \frac{\partial w}{\partial z},\ \frac{1}{2}\left(\frac{\partial u}{\partial y} + \frac{\partial v}{\partial x}\right),\ \frac{1}{2}\left(\frac{\partial v}{\partial z} + \frac{\partial w}{\partial y}\right),\ \frac{1}{2}\left(\frac{\partial w}{\partial x} + \frac{\partial u}{\partial z}\right)\right]^T \tag{8}$$

Downloaded from https://www.cambridge.org/core. 11 Nov 2026 at 09:59:05, subject to the Cambridge Core terms of use.

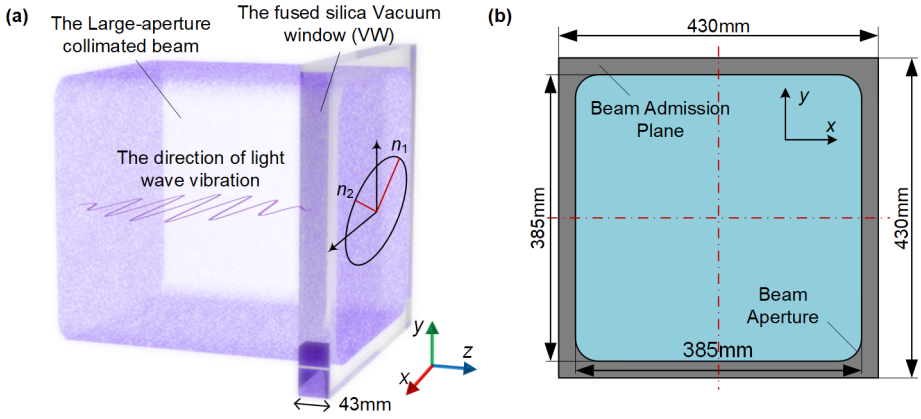


Figure 2. **(a)** The propagation direction, integrated thickness, and refractive index ellipsoid cross section of a large-aperture laser beam within the fused silica vacuum window. **(b)** The clear aperture geometry of the VW and the effective beam aperture of the large-aperture laser beam.

The nodal displacements within the medium give rise to variations in the internal stress state. According to Hooke's law, the relationship between stress and strain in the material can be expressed through the generalized constitutive matrix:

$$\boldsymbol{\sigma} = \frac{\lambda_{\text{Lame}}}{\mu} \cdot \begin{bmatrix} c_{11} & c_{12} & c_{12} & 0 & 0 & 0 \\ c_{12} & c_{11} & c_{12} & 0 & 0 & 0 \\ c_{12} & c_{12} & c_{11} & 0 & 0 & 0 \\ 0 & 0 & 0 & c_{44} & 0 & 0 \\ 0 & 0 & 0 & 0 & c_{44} & 0 \\ 0 & 0 & 0 & 0 & 0 & c_{44} \end{bmatrix} \cdot \boldsymbol{\varepsilon} \tag{9}$$

Where λ_{Lame} is the Lamé constant of the material, given by $\lambda_{\text{Lame}} = \frac{E\,\nu}{(1+\nu)(1-2\nu)}$, where E is Young's modulus and ν is Poisson's ratio. The reduced stiffness coefficients are defined as $c_{11} = 1-\nu$, $c_{12} = \nu$, and $c_{44} = (c_{11}-c_{12})/2$. Under external loading, the static equilibrium of the medium is governed by the Cauchy equilibrium equations in the Cartesian coordinate system:

$$\begin{aligned} \sum F_x &= \frac{\partial \sigma_x}{\partial x} + \frac{\partial \tau_{xy}}{\partial y} + \frac{\partial \tau_{zx}}{\partial z} + f_x = 0 \\ \sum F_y &= \frac{\partial \tau_{xy}}{\partial x} + \frac{\partial \sigma_y}{\partial y} + \frac{\partial \tau_{yz}}{\partial z} + f_y = 0 \\ \sum F_z &= \frac{\partial \tau_{zx}}{\partial x} + \frac{\partial \tau_{yz}}{\partial y} + \frac{\partial \sigma_z}{\partial z} + f_z = 0 \end{aligned} \tag{10}$$

By employing the three fundamental equations of linear elasticity together with mechanically appropriate boundary conditions, the governing differential equations can be solved to obtain the physical quantities of interest.

2.2.2. *Boundary Conditions and Loading Configuration*

Given the structural configuration of the VW, when the edge load is approximately uniform across the thickness, the x–y plane stress tensor field remains identical at any integration plane along the thickness direction. Under this condition, the refractive-index-related parameters become independent of the integration position and reduce to thickness-invariant quantities. Consequently, it is only necessary to analyze how the functional distribution of the edge load along the clear aperture direction affects the x–y plane stress tensor field. Owing to the structural symmetry of the loading condition, the edge stress load distribution can be defined as:

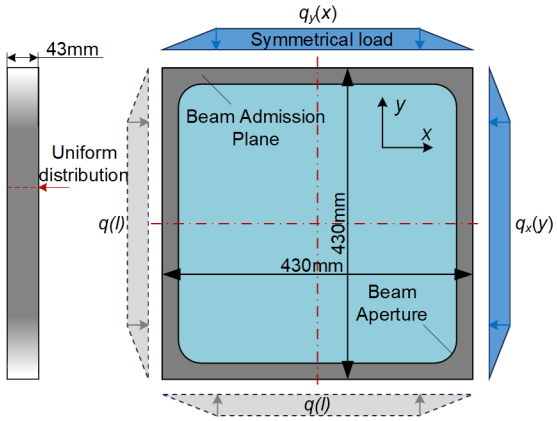


Figure 3. Schematic of the application direction of symmetric edge pressure loads.

$$\begin{cases} x = \pm D/2: & \sigma_{xx} = q_x(y),\ \sigma_{xy} = 0 \\ y = \pm L/2: & \sigma_{yy} = q_y(x),\ \sigma_{xy} = 0 \end{cases} \tag{11}$$

Here, D and L denote the clear aperture dimensions of the optical element, with $D = L = 430$ mm in the present study. The functions $q_x(y)$ and $q_y(x)$ represent the edge pressure distributions along the corresponding boundaries, satisfying $q_x(y) = q_y(x) = q(l)$. The function $q(l)$ is an even-symmetric stress distribution with respect to the symmetry axis, i.e., $q(l) = q(-l)$, as illustrated in Fig. 3.

Downloaded from https://www.cambridge.org/core. 11 Nov 2026 at 09:59:05, subject to the Cambridge Core terms of use.

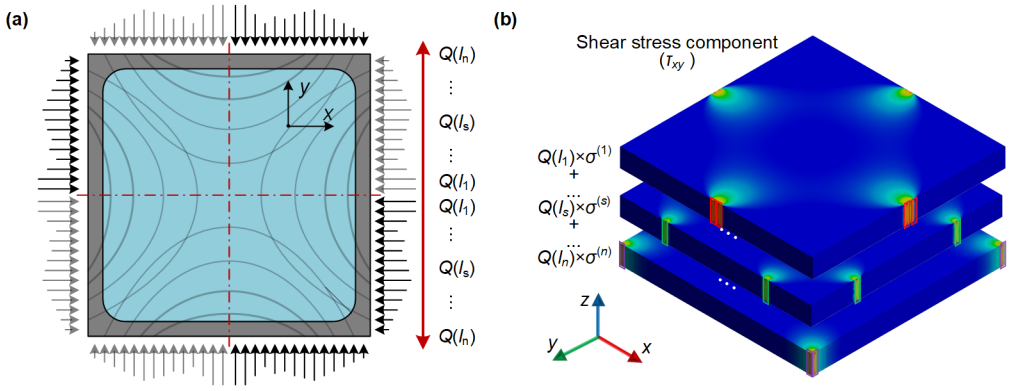


Figure 4. **(a)** Discretization of boundary conditions. **(b)** Linear combination of unit pressure loads.

2.2.3. *Discrete Solution of the Stress Tensor Field*

Under non-uniform pressure loading, closed-form analytical solutions generally do not exist for the three-dimensional or plane stress tensor fields in large-aperture optical elements. The finite element method (FEM), as a mature and versatile numerical approach, enables the effective discretization and solution of complex mechanical models. Therefore, in this work, FEM is employed to perform the mechanical analysis of the optical element. For large-aperture laser beams, the plane stress tensor fields induced by different mechanical boundary conditions result in varying degrees of optical modulation. Consequently, a comprehensive analysis of various boundary configurations is essential. However, simulating the mechanical responses associated with all possible boundary conditions is computationally prohibitive. Within the scope of linear elasticity, the relationship between boundary conditions and the mechanical response of the medium constitutes a linear system. Therefore, if the input boundary condition is a linear combination of two or more functions, the output response is equal to the linear combination of the outputs generated by each individual input function. Within the clamping-force range considered in this study, the fused silica element remains in the linear elastic regime, and the calculated stress levels are far below the tensile and compressive strength limits of the material. Therefore, the mechanical response can be described using the principle of linear superposition. By exploiting the superposition principle, an arbitrary symmetric input boundary condition $q(l)$ distributed over the aperture can be discretized, and the total load within the stressed region can be expressed as:

$$F = 2 \sum_{n=1}^{L/(2\Delta l)} Q(l_n)\, q_0\, d\Delta l \tag{12}$$

Here, Q denotes the load amplitude at position l_n, q_0 is the response function for a unit load, and Δl represents the discretization interval of the load distribution (see Fig. 4(a)). For this unit load q_0, the finite element method is employed to compute the stress tensor field $\boldsymbol{\sigma}_0^{(n)}$ induced when the pressure acts at the n-th discrete point. For fused silica elements operating within the elastic regime, the constitutive relations, geometric compatibility, and boundary conditions all satisfy the linearity assumption. Consequently, the total stress tensor field response induced by the symmetric load $q(l)$ over the entire boundary is equal to the linear superposition of the responses generated by each discretized unit load q_0 acting independently within its respective subinterval $(l_n, l_n + \Delta l)$ (see Fig. 4(b)). Therefore, the total discretized stress tensor field response of the fused silica element under the symmetric load $q(l)$ in the linear elastic regime is defined as:

$$\boldsymbol{\sigma}^{(\text{total})} = \sum_{n=1}^{L/(2\Delta l)} Q(l_n) \cdot \boldsymbol{\sigma}_0^{(n)} \tag{13}$$

Consequently, we have established the coupled finite element discretization model linking the stress tensor field of the large-aperture fused silica transmission element to its boundary conditions.

2.3. *Propagation Model and BP Algorithm for the High-Power Beam*

2.3.1. *Stress-Informed Beam Propagation Model*

In the (ICF) driver, the front-end system must perform energy amplification, spatial shaping, filtering, and frequency conversion ($1\omega \rightarrow 3\omega$) for large-aperture beams. This necessitates maintaining a high degree of linear polarization purity. Consequently, a mechanically stressed VW is strategically positioned in the third-harmonic beam path to tailor the beam's polarization state. Fig. 5 shows the primary optical components and the beam propagation process in the third-harmonic section of the FOA. The spatial propagation model for large-aperture beams is formulated as comprising the following three parts:

Step 1: Initial Beam Definition and Phase Modulation by the CPP

When the beam propagates to the front surface of the

Downloaded from https://www.cambridge.org/core. 11 Nov 2026 at 09:59:05, subject to the Cambridge Core terms of use.

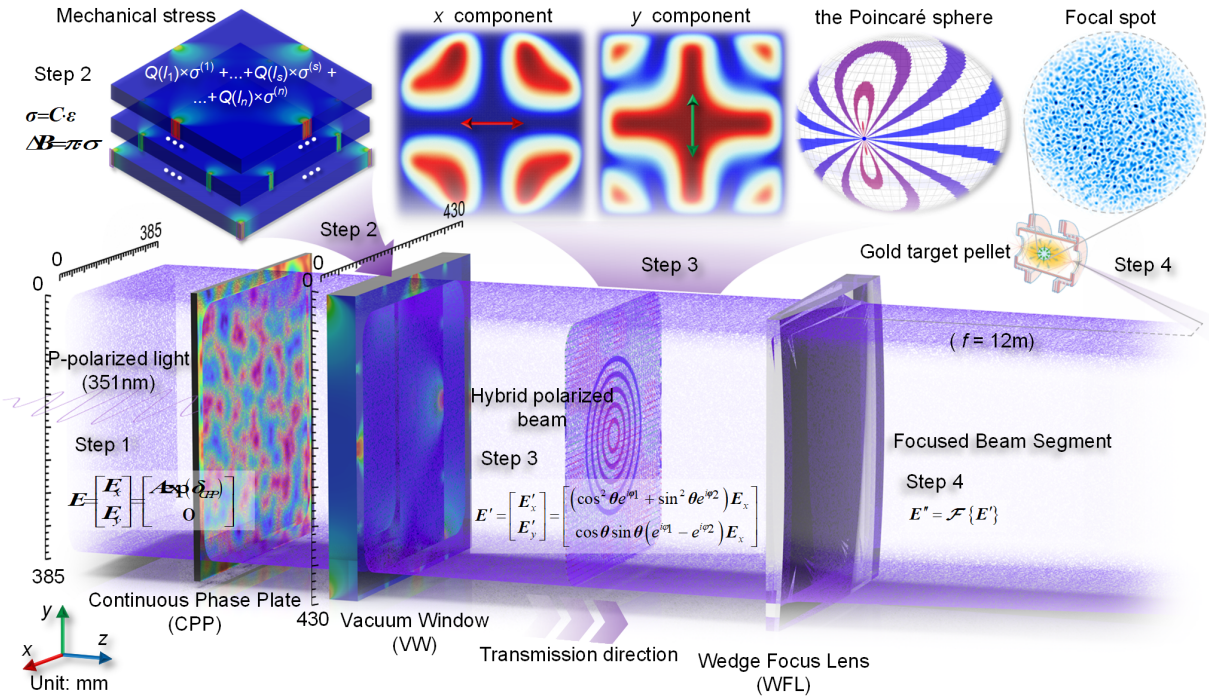


Figure 5. Partial propagation of a large-aperture beam in the final optics assembly (FOA).

continuous phase plate (CPP), it is assumed to be a collimated, large-aperture, super-Gaussian, P-polarized vector beam with the wavelength of 351 nm and a uniform phase distribution. This assumption is valid because the beam has undergone rigorous shaping and filtering in the front-end optical path.

As light waves are complex amplitude vectors encompassing amplitude, phase, and vibration direction, direct modeling is computationally intensive. In beam tracing algorithms, the wave is decomposed along orthogonal axes into two orthogonally polarized complex amplitude components based on its vibration characteristics. Consequently, the vector complex amplitude distribution at the front surface of the CPP in high-power laser systems can be defined in Cartesian coordinates as:

$$\boldsymbol{U}_0(x,y) = \begin{bmatrix} \boldsymbol{U}_{x0}(x,y) \\ \boldsymbol{U}_{y0}(x,y) \end{bmatrix} = \begin{bmatrix} A(x,y)e^{i\varphi_0(x,y)} \\ 0 \end{bmatrix} \tag{14}$$

$$A(x,y) = A_0 \exp\left(-\left(\left(\frac{2x}{L_1}\right)^2\right)^n + \left(\left(\frac{2y}{D_1}\right)^2\right)^n\right) \tag{15}$$

Here, $\varphi_0(x,y)$ denotes the initial phase field of the beam. Under the condition of a uniform phase distribution, $\varphi_0(x,y)$ is set to zero. L_1 and D_1 represent the beam aperture dimensions, with $L_1 = D_1 = 385$ mm. The electric field amplitude peak A_0 is determined jointly by the laser energy P and the pulse width τ_p, where $P = 2000$ J and $\tau_p = 3$ ns. The parameter n is the order of the super-Gaussian function, taken as $n = 8$.

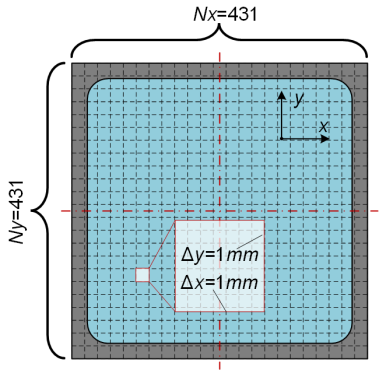


Figure 6. The matrix discretization scheme for the beam and optical elements.

In the model calculation, various physical quantities of the optical field are subjected to matrix-based discretization. As illustrated in Fig. 6, a two-dimensional optical field matrix is established on the beam cross-section, featuring a sampling interval of 1 mm and a total sampling size of 431 × 431. Similarly, subsequent optical elements in the path, such as the CPP and the VW, are also modeled using this matrix-based representation to achieve their numerical simulation.

The CPP is fabricated using precision mechanical grinding, resulting in a continuously varying surface profile designed to impose a phase modulation on the incident beam. Upon transmission through the element, a specific continuous phase distribution function $T_1 = \delta_{\mathrm{CPP}}(x,y)$ is introduced into the complex amplitude vector field of the beam. Consequently,

Downloaded from https://www.cambridge.org/core. 11 Nov 2026 at 09:59:05, subject to the Cambridge Core terms of use.

the transmitted field satisfies:

$$\boldsymbol{U}_1(x,y;0)=\begin{bmatrix}\boldsymbol{U}_{1x}(x,y)\\ \boldsymbol{U}_{1y}(x,y)\end{bmatrix}=\begin{bmatrix}\boldsymbol{U}_{0x}(x,y)e^{i\delta_{CPP}(x,y)}\\ 0\end{bmatrix} \quad (16)$$

After being modulated by the CPP, the beam undergoes free-space diffraction prior to reaching the downstream optical element. To circumvent the complexity of directly solving the diffraction integral, the angular spectrum theory is employed to transform the propagation analysis from the spatial domain into the frequency domain. According to this theory, any complex optical wave can be decomposed into a linear superposition of plane-wave components (i.e., angular spectra) with different weighting coefficients. Consequently, the angular spectrum of the propagating field immediately after the CPP can be expressed as:

$$\boldsymbol{A}_1(f_x,f_y)=\iint_{-\infty}^{\infty}\boldsymbol{U}_1(x,y)\times\exp\left[-i2\pi\left(f_x x+f_y y\right)\right]dx\,dy \quad (17)$$

Here, $f_x=\alpha/\lambda$ and $f_y=\beta/\lambda$ denote the spatial frequencies corresponding to the direction cosines (α,β). Upon propagating a distance z in free space, each plane-wave component accumulates a phase delay characterized by the transfer function $H(f_x,f_y,z)$, which is expressed as:

$$\boldsymbol{A}_1(f_x,f_y;z)=\boldsymbol{A}_1(f_x,f_y)\,\boldsymbol{H}(f_x,f_y;z) \quad (18)$$

$$\boldsymbol{H}=\begin{cases}e^{ikz\sqrt{1-(\lambda f_x)^2-(\lambda f_y)^2}}, & f_x^2+f_y^2<1/\lambda^2\\ 0, & Other\end{cases} \quad (19)$$

Here, $k=2\pi/\lambda$ denotes the wavenumber. By performing a two-dimensional inverse Fourier transform on the propagated angular spectrum, the field is reconstructed back into the spatial domain, yielding the complex amplitude distribution at the observation plane:

$$\boldsymbol{U}_1(x,y;z)=\int_{-\infty}^{\infty}\int_{-\infty}^{\infty}\boldsymbol{A}_1(f_x,f_y;z)\times\exp\left[i2\pi\left(f_x x+f_y y\right)\right]df_x df_y \quad (20)$$

For discretized optical fields represented in matrix form, the two-dimensional Fast Fourier Transform (2D-FFT) is typically employed for numerical analysis. Regarding the image field at the observation plane following transmission through subsequent optical elements, the spatial propagation algorithm described above is uniformly adopted to obtain the solution.

Step 2: Stress-Induced Optical Modulation

Under the action of edge pressure clamping, the stress tensor field is numerically discretized, yielding the phase retardation distribution $\delta(x,y)$ and the fast-axis azimuth $\theta(x,y)$ for the VW operating at 351 nm. Within the VW, the incident complex amplitude vector field is decomposed in the rotated coordinate system (x',y') into two orthogonal components: $U_{1x'}(x',y';z_1)$ and $U_{1y'}(x',y';z_1)$. Here, the rotation angle of the new coordinate system relative to the original one is $\theta(x,y)$. In this local frame, $U_{1x'}$ and $U_{1y'}$ correspond to vibrations along the slow and fast axes, respectively. Upon traversing the VW, a phase retardation distribution $\delta(x,y)$ is induced between the emergent complex amplitude components $U_{2x'}$ and $U_{2y'}$. Subsequently, the field U_2 at the observation plane must be transformed back to the original coordinate system. The transmission process described above can be mathematically represented by the Jones matrix field $\mathbf{J}(x,y)$ as follows:

$$\boldsymbol{U}_2(x,y;0)=\begin{bmatrix}\boldsymbol{U}_{2x}(y;0)\\ \boldsymbol{U}_{2y}(x,y;0)\end{bmatrix}=\boldsymbol{J}(x,y)\begin{bmatrix}\boldsymbol{U}_{1x}(x,y;z_1)\\ \boldsymbol{U}_{1y}(x,y;z_1)\end{bmatrix} \quad (21)$$

$$\boldsymbol{J}=\begin{bmatrix}\cos\boldsymbol{\theta} & -\sin\boldsymbol{\theta}\\ \sin\boldsymbol{\theta} & \cos\boldsymbol{\theta}\end{bmatrix}\begin{bmatrix}1 & 0\\ 0 & e^{i\boldsymbol{\delta}}\end{bmatrix}\begin{bmatrix}\cos\boldsymbol{\theta} & \sin\boldsymbol{\theta}\\ -\sin\boldsymbol{\theta} & \cos\boldsymbol{\theta}\end{bmatrix} \quad (22)$$

For brevity, the fast-axis orientation distribution $\theta(x,y)$ and the phase retardation distribution $\delta(x,y)$ are hereafter abbreviated as $\boldsymbol{\theta}$ and $\boldsymbol{\delta}$, respectively. In the Jones matrix $\boldsymbol{J}$, the first and third terms correspond to the forward and inverse coordinate transformation operators between the original and the rotated coordinate systems, respectively. The second term represents the phase retardation modulation applied to the two orthogonal polarization components within the rotated frame.

Step 3: Far-Field Beam Propagation

The modulated beam propagates through free space to the wedge lens and is focused onto the target observation plane. Based on the Huygens-Fresnel principle and under the paraxial approximation, the relationship between the far-field $U_3(x_f,y_f;f)$ and the near-field $U_2(x,y;z_2)$ in front of the lens can be expressed as:

$$\boldsymbol{U}_3(x_f,y_f;f)=\frac{e^{ijf}}{i\lambda f}\iint_{-\infty}^{\infty}\boldsymbol{U}_2(x,y;z_2)\times\exp\left[-i\frac{2\pi}{\lambda f}(x_f x+y_f y)\right]dx\,dy \quad (23)$$

Where f is the focal length of the lens; x_f,y_f are the spatial coordinates of the observation plane; $e^{ikf}/(i\lambda f)$ is a complex constant factor that does not affect the analysis of the relative light intensity distribution. Thus, $U_3(x_f,y_f;f)\propto\mathcal{F}\{U_2(x,y;z_2)\}$, where $\mathcal{F}$ denotes the Fourier transform, $x_f=\lambda f\cdot\xi$ and $y_f=\lambda f\cdot\eta$, with ξ and η being the spatial frequencies after the 2D Fourier transform.

Downloaded from https://www.cambridge.org/core. 11 Nov 2026 at 09:59:05, subject to the Cambridge Core terms of use.

At the defocused observation plane located at a distance z_3 ($z_3 \neq f$) from the lens, the far-field distribution is given by $U_3(x_f, y_f; z_3) \propto \mathcal{F}\{U_2'(x, y; z_2)e^{iB}\}$, where B is the additional quadratic phase factor introduced by the defocused plane:

$$B = \pi \frac{(f - z_3)(x^2 + y^2)}{\lambda f z_3} \tag{24}$$

For the complex amplitude vector field, we apply 2D-FFT to each of its orthogonal components to solve for the focused field distribution. In summary, the complete physical model describing the spatial propagation and focusing of large-aperture beams through the CPP, VW, and lens has now been established. Regarding the intensity distribution during propagation, it is defined by $I(x, y) = U(x, y) \cdot U^*(x, y)$. Under discretized matrix conditions, $I(x, y)$ must be normalized to ensure energy conservation, and the actual peak intensity (in $\mathrm{W/cm^2}$) is then determined based on the total laser energy P and pulse width τ_p:

$$I_{\text{real}}(x, y) = \frac{P}{\tau_p \Delta x \Delta y} \frac{I(x, y)}{\sum_{n=x,y} I(x, y)} \tag{25}$$

where Δx and Δy are the sampling intervals in the spatial domain, with units of cm.

2.3.2. BP Algorithm under Mechanical Constraints

In Section 2.2, the solution method was established for the total stress tensor field $\boldsymbol{\sigma}^{(\text{total})}$ under arbitrary symmetric boundary loads $q(l)$. This stress field directly governs the birefringence parameter distribution of the VW and modulates the optical transmission characteristics of the beam in subsequent spaces. This subsection aims to address an inverse design problem: given a desired field distribution function in the target region, how to optimize the preload applied to the fixture. To achieve this, a backward propagation algorithm integrating the optical field transmission model and physical boundary constraints is introduced. The core concept involves constructing the entire mechanical-optical transmission chain as a differentiable computational graph. By leveraging automatic differentiation, the gradient of the intensity loss function in the target region is back-propagated to the input preload, enabling end-to-end optimization. The construction procedure for the large-aperture beam backward propagation algorithm, considering physical boundary constraints, is as follows:

Step 1: Parameter Tuning under Mechanical Constraints

The stress tensor field responsible for beam modulation is generated by the edge pressure of the VW, which must be applied through realistic physical constraints. For mechanically clamped stress regulation, factors such as the contact configuration between the optic and the fixture, as well as the location and magnitude of the preload, all influence the edge pressure. Therefore, a mapping between the preload parameters and the edge load can be defined as follows:

$$q(l) = \Gamma\{\boldsymbol{F}(p_1, \ldots, p_n)\} \tag{26}$$

Here, $\boldsymbol{F}(p_1, \ldots, p_n)$ denotes the preload force, where $p_1, \ldots, p_n$ are the parameters governing its characteristics.

Step 2: Forward Model Construction

In Section 2.3.1, a beam propagation model for high-power laser facilities was constructed, taking the initial field function and mechanical boundary conditions as inputs, and yielding the field distribution at any observation plane. In the ICF, the intensity distribution at the focal plane serves as the critical metric for evaluating the effectiveness of polarization smoothing. Therefore, we adopt the intensity at the focal observation plane, $I_3(x_f, y_f; f)$, as the output of the forward model. By integrating the relationship between the preload and the edge pressure established in Step 1, we can construct the forward computational model that takes the preload parameter $\boldsymbol{F}(p_1, \ldots, p_n)$ as its input:

$$I(x_f, y_f; f) = \text{forward}\{p_1, \ldots, p_n\} \tag{27}$$

Step 3: Loss Function Definition

The optimization objective is to make the predicted intensity $I(x_f, y_f; f)$ as close as possible to the desired intensity $I_{\text{goal}}(x_f, y_f; f)$. We can define the loss function as the Root Mean Square Error (RMSE) between the predicted and target intensity distributions:

$$\mathcal{L}(\boldsymbol{F}) = \frac{1}{NM} \sum_{n=x_f}^{N} \sum_{m=y_f}^{M} \left[I(x_f, y_f; f) - I_{\text{goal}}(x_f, y_f; f) \right]^2 \tag{28}$$

Step 4: Backpropagation via Automatic Differentiation

For the preload parameter $\boldsymbol{F}(p_1, \ldots, p_n)$, the objective is to find the optimal set $\{p_1, \ldots, p_n\}$ that minimizes the loss function $\mathcal{L}(\boldsymbol{F})$. Utilizing the backpropagation algorithm, partial derivatives of each node tensor with respect to its associated nodes are computed layer-by-layer in reverse order from the output layer, ultimately yielding the gradient of the loss function $\mathcal{L}(\boldsymbol{F})$ with respect to the preload parameter $\nabla_{\boldsymbol{p}}\mathcal{L}$. Leveraging this gradient information, the updated preload parameters corresponding to the next iteration step can be derived as follows:

$$\boldsymbol{F}_{\text{new}} = \boldsymbol{F}_{\text{old}} - \chi \cdot \nabla_p \mathcal{L} \tag{29}$$

Where χ denotes the learning rate.

Downloaded from https://www.cambridge.org/core. 11 Nov 2026 at 09:59:05, subject to the Cambridge Core terms of use.

3. Results and discussion

3.1. Parameter Reduction under Mechanical Constraints

In the mechanical clamping scheme for stress-modulated polarization smoothing, the VW is seated within the clamping frame, with longitudinal shims and copper plates interposed between the frame and the window. A centralized preload is applied to the central region of the window via a setscrew acting on the outer midsection of the copper plate; whereas symmetrically distributed preloads in the non-central regions of the copper plate are generated using wedge.

Once the preload application structure is fixed, the material parameters of the shims interposed between the optical element and the frame become a critical factor governing the edge pressure distribution on the element. Numerical simulations indicate that the pressure exerted on the optic edge by the preload, after being transferred through the copper plate and intermediate shims, exhibits a high degree of conformity with a Gaussian profile. As shown in Fig. 7(a) and 7(b), we assigned different Young's moduli and Poisson's ratios to the shims to mimic four common optical contact materials: silicone, F246 rubber, ABS plastic, and copper. These materials form a stiffness gradient from soft to rigid, covering the range of contact media typically used in optical alignment. Fig. 7(c) provides the comprehensive schematic illustrating the layout of the preload application points, the composite structure of the fixture materials, and the resultant edge pressure distribution. Fig. 7(d) shows the edge pressure distribution induced by a 1000-N preload applied at the center of the clamping surface (corresponding to position NO.10 in Fig. 7(c)). It can be observed that the pressure distribution at the optic interface exhibits a good fit to the Gaussian profile across all selected intermediate contact materials with varying stiffness. Furthermore, the standard deviation of the pressure distribution, σ_{gauss}, decreases as the stiffness of the contact material increases. This implies that for a constant preload, a higher stiffness results in a narrower and more peaked pressure distribution at the optic interface. The relationship between the preload and the edge pressure distribution can be expressed as:

$$F_s = A \cdot d \cdot \sigma_{gauss} \sqrt{2\pi} \cdot \left[\Phi\left(\frac{-l/2 - \mu}{\sigma_{gauss}} \right) - \Phi\left(\frac{l/2 - \mu}{\sigma_{gauss}} \right) \right] \quad (30)$$

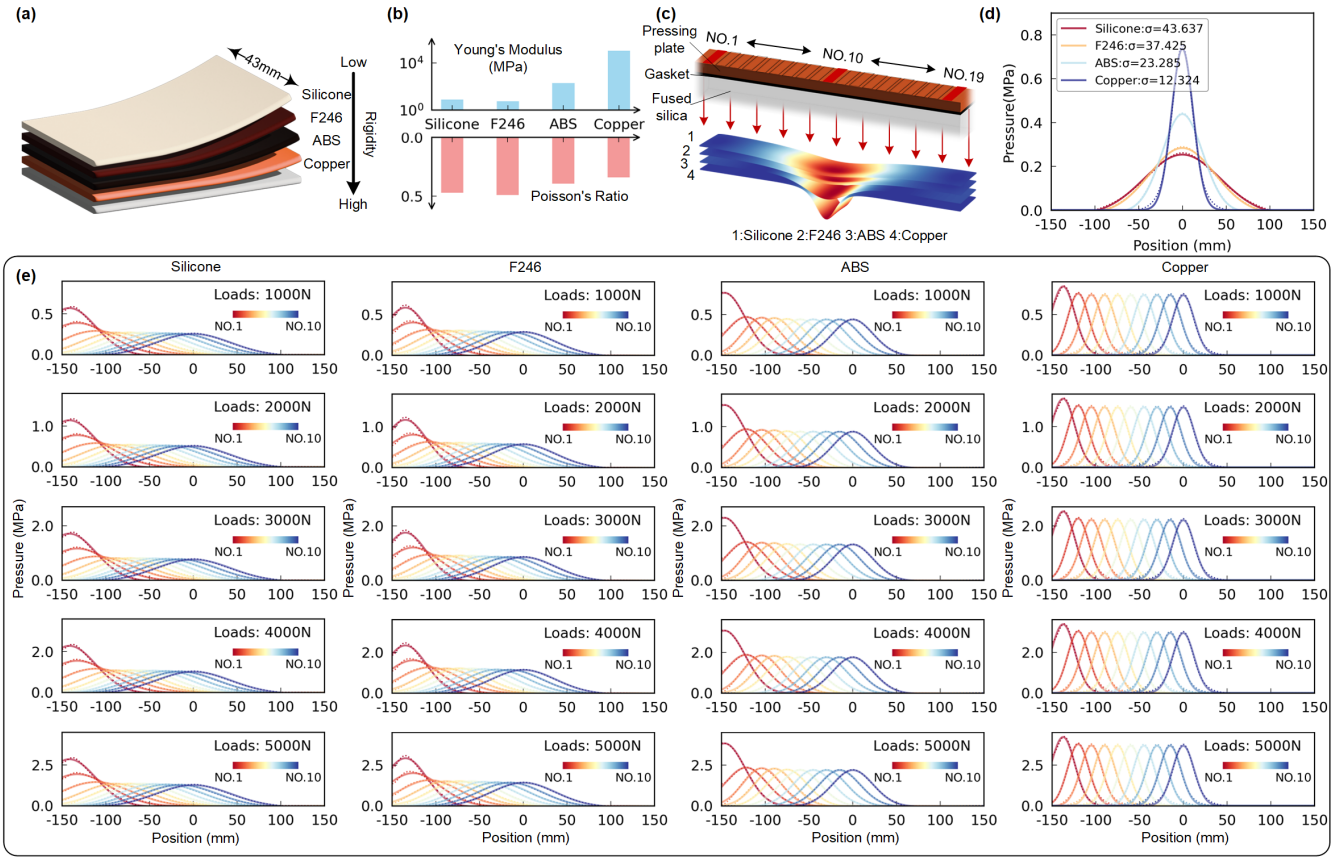


Figure 7. **(a)** Schematic of the four contact structures with varying stiffness (d = 43 mm). **(b)** Mechanical properties of the contact materials. **(c)** Schematic of the preload application points on the copper plate and the contact configuration. **(d)** Edge pressure distributions and Gaussian fitting results for the four materials under the preload at position NO.10. **(e)** Edge pressure distributions for the four materials under various preload positions and magnitudes.

Downloaded from https://www.cambridge.org/core. 11 Nov 2026 at 09:59:05, subject to the Cambridge Core terms of use.

Here, F_s denotes the preload magnitude, A is the pressure amplitude constant associated with the Gaussian distribution, Φ represents the integral function of the standard normal distribution. To verify the consistency of this fitting method across arbitrary edge positions and preload magnitudes, preload tests were conducted at locations NO.1 to NO.19 for all four contact materials. Exploiting structural symmetry, only the simulation results for positions NO.1 to NO.10 are presented here. As shown in Fig. 7(e), the pressure distributions induced by the preload at various locations all exhibit a good Gaussian fit. Furthermore, the peak pressure increases as the loading position shifts toward the edges. This occurs because the positional shift reduces the mean μ in Eq. (30), lowering the integral value of the standard normal distribution Φ over the interval. Consequently, to maintain a constant preload magnitude F_s, the pressure amplitude constant A in the equation must increase accordingly. The comparison of the edge pressure distributions at the same loading location under different preload magnitudes F_s reveals that varying F_s only scales the overall amplitude of the distribution linearly, without altering its underlying shape.

Based on the relationship between the preload and the edge pressure distribution established above, the preload parameters (F_s, P) can be mapped to the Gaussian distribution parameters $(A, \mu, \sigma_{\text{gauss}})$ induced by the intermediate medium. For the preload applied by the central setscrew on the copper plate, the induced pressure parameters are characterized as $(A_1, \mu_1 = 0, \sigma_{1\text{gauss}})$. For the symmetric off-center preloads generated by the two wedges, the corresponding pressure parameters are given by $(A_2, \mu_2 = \pm P, \sigma_{2\text{gauss}})$. Since both loading configurations share the same shim contact material, we have $\sigma_{1\text{gauss}} = \sigma_{2\text{gauss}} = \sigma_{\text{gauss}}$. Consequently, the edge pressure distribution under the frame preload boundary constraint can be reduced to four independent parameters: Para = $(A_1, A_2, P, \sigma_{\text{gauss}})$.

3.2. Optimization Results of Edge Pressure and Preload

Based on the beam propagation model described in Section 2.3.2, we constructed the optical transmission system class to simulate the sub-beam propagation process under stressed operating conditions. This class encapsulates all the beam and optical component models required to execute the optimization algorithm. As shown in Fig. 8 (a), the test pulse was initialized with the energy = 2000 J, the wavelength = 351 nm, the order = 8, the pulse width = 3 ns, and P-polarization. During propagation, the test pulse is subjected to a predefined random continuous phase distribution to simulate the phase modulation effect induced by CPP. After propagating a certain distance, the phase-modulated pulse undergoes subsequent polarization modulation. Since the initialization of the test pulse and the CPP phase modulation strategy are fixed, they are uniformly treated as constants within the optimization algorithm framework. In the variable layer, the parameters governing the edge pressure distribution, Para = $(A_1, A_2, P, \sigma_{\text{gauss}})$, are defined as design variables and assigned to Input Layer 1. Within the forward calculation framework, the design variables in the input layer directly govern the material optical parameters of each PS node. As the test pulse propagates through the stressed optical component, its polarization state (vibration direction) and phase are altered at each node accordingly. After modulation by the PS nodes, the test pulse propagates through free space and undergoes convolution transformation before reaching the lens node. Following focusing by the lens, the pulse arrives at the focal spot target layer. In the target layer, the algorithm will evaluate the uniformity of the focal spot energy distribution by comparing the desired target with the calculated results, and subsequently feeds back the deviation for optimization. The optimization framework is constructed based on tensor operations. During forward propagation, the gradients of all associated nodes are computed automatically. Following the error evaluation in the target layer, backward optimization is performed using these gradient values.

The flat-top beam exhibits a uniform spatial energy distribution (RMS = 0) across the spot region, making it an ideal reference for optimizing the uniformity of the focal spot energy distribution. In fact, the focal spot generated by the CPP-modulated pulse consists of numerous fine-scale speckles with non-uniform energy distribution, which significantly increases the RMS value. The PS technique effectively suppresses these speckles, leading to a notable reduction in the RMS of the focal spot. By adopting a flat-top beam as the target energy distribution, the reduction in focal spot RMS induced by different stress distributions can be effectively quantified. As shown in Fig. 8(b), we define a super-Gaussian circular beam with order = 8 to approximate the flat-top beam profile. The characteristic radius of this beam is set equal to the radius of the CPP-shaped focal spot. By adjusting the energy amplitude constant to fix the total energy at 2000 J, the target distribution for the optimization algorithm is defined. Under the constraints of the objective function, we can optimize the edge pressure by updating the gradient fields of the associated nodes via backpropagation. During the optimization process, all parameters in the set Para are normalized to ensure a consistent sampling step size across all dimensions. Fig. 8(c) illustrates the edge pressure distribution when the focal spot RMS converges after multiple iterations of optimization. The optimal configuration is achieved when the symmetric preloads at positions ±50.78 mm yield a peak edge pressure of 1.88 MPa, the central preload at 0 mm yields 0.85 MPa, and the material parameter σ_{gauss} = 30.01 mm. Under this condition, the relative contrast of the focal spot is reduced by a factor of 0.77 relative to that obtained using the CPP alone.

Regarding the internal stress of the component, the principal stress induced by the edge pressure decays with increasing distance from the load source, asymptotically approaching zero. The stress gradient concurrently diminishes, and the rate

Downloaded from https://www.cambridge.org/core. 11 Nov 2026 at 09:59:05, subject to the Cambridge Core terms of use.

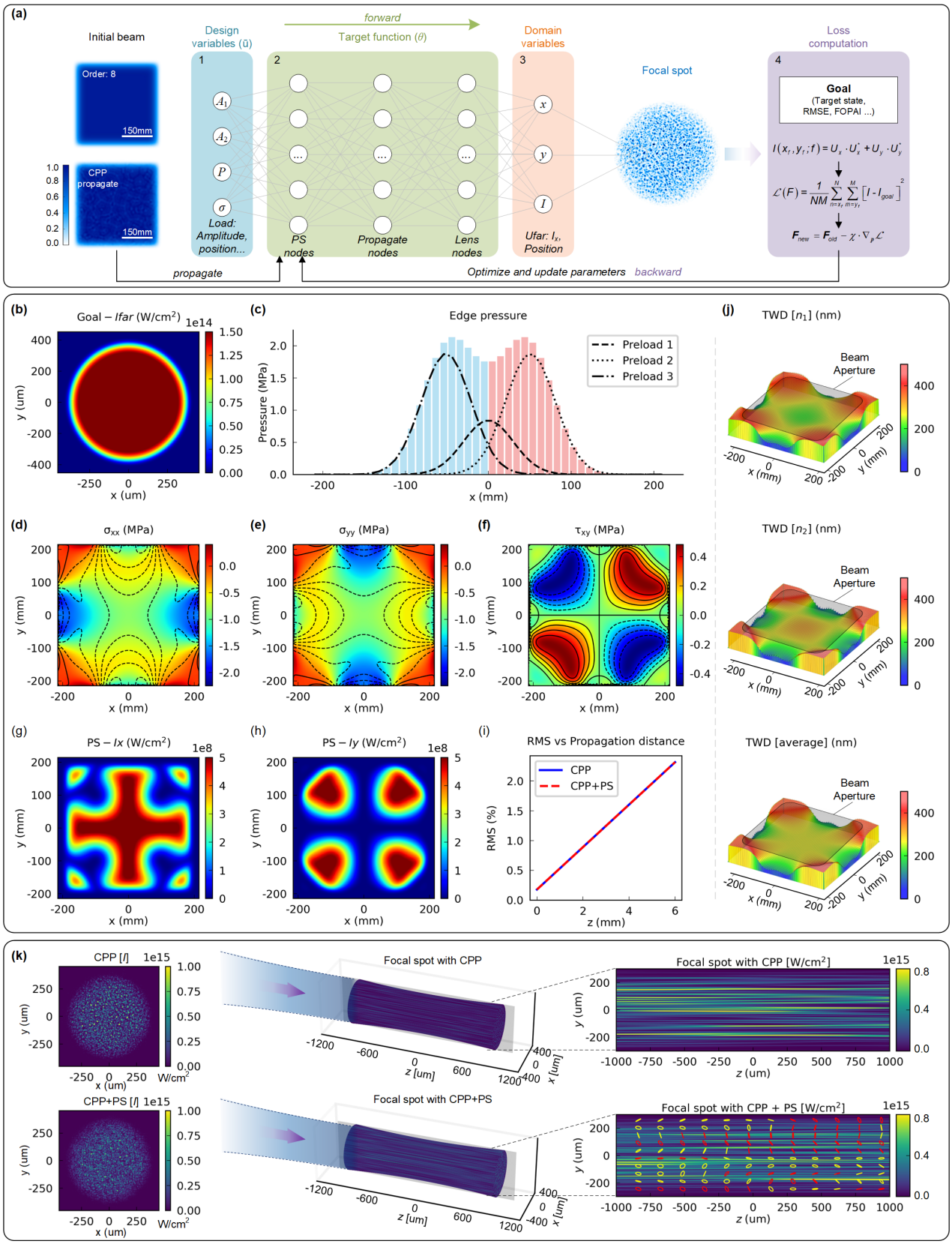


Figure 8. **(a)** The iterative optimization framework based on the gradient descent BP algorithm. **(b)** The desired target energy distribution. **(c)** Optimized preload parameters and the corresponding edge pressure profile. **(d)–(f)** Internal stress distributions induced by edge pressure: normal stresses (σ_{xx}, σ_{yy}) and shear stress (τ_{xy}). Normal stress is defined as negative for compression and positive for tension; shear stress is defined as positive for counter-clockwise shear and negative for clockwise shear. **(g)–(h)** Near-field energy distributions of the polarization components for the test pulse under stress modulation. **(i)** RMS curves characterizing the energy uniformity during near-field pulse propagation. **(j)** Transmission wavefront distortion induced by internal stress. **(k)** Energy distributions in the far-field focal plane and near the focus.

Downloaded from https://www.cambridge.org/core. 11 Nov 2026 at 09:59:05, subject to the Cambridge Core terms of use.

of this decay is governed by the geometric dimensions of the element. For the VW with dimensions of 430 mm × 430 mm, the internal stress component distributions under the optimized edge pressure are illustrated in Figs. 8(d)–8(f). The pressure distribution generates two zones of high normal stress near the edges of the optical aperture, with the stress values gradually decreasing toward the center of the component. In the corner regions of the element, where the edge pressure is relatively low, the normal stress is nearly absent. Under the combined action of the edge pressure units, the shear stress exhibits a shield-shaped gradient pattern symmetrically distributed across the four quadrants. The size of these sub-regions, the gradient distribution, and the spacing between them are determined by both the locations and magnitudes of the preloads. The modulation effect of the internal stress distribution induced by edge pressure on the near-field energy distribution of the test pulse is illustrated in Figs. 8(g) and 8(h). The internal stress tensor field induces partial polarization conversion from the initial P-state to the S-state within the test pulse aperture. The spatial distribution and conversion ratio of this effect exhibit a strong correlation with the gradient distribution of the shear stress components. The configuration of the edge pressure units spatially isolates the converted S-polarized components, interleaving them with the residual P-polarized regions. This distribution pattern effectively reduces the overlap area among far-field polarization speckles, thereby providing a significant positive gain for the incoherent superposition of focal spot components. Additionally, numerical simulations were conducted to characterize the wavefront phase modulation induced by the stress tensor field and the resulting intensity redistribution during propagation. As shown in Fig. 8(j), the variations in the refractive indices of the fast and slow axes induced by the stress tensor field result in transmission wavefront distortions TWD$[n_1]$ and TWD$[n_2]$ for the beam components vibrating along these axes, with peak values of 438 nm and 517 nm, respectively. The overall transmission wavefront distortion of the beam vector field is characterized by the average of the distortions of the two components, denoted as TWD[average]. Under stress loading, the peak TWD[average] of the beam vector field reaches 478 nm ($\approx 1.36\lambda$). Furthermore, the gradient change from the peak to the valley is gradual, with no abrupt transitions observed. Fig. 8(i) plots the evolution of the RMS value for the beam modulated by both CPP and PS at various propagation distances z. The results indicate that the impact of the phase modulation introduced by CPP on the beam energy distribution intensifies progressively with increasing propagation distance; however, the RMS curves for the CPP-only and CPP+PS cases exhibit a high degree of coincidence. This confirms that the stress-induced transmission wavefront distortion does not induce any adverse energy modulation effects on the beam. Consequently, the beam maintains good optical uniformity during near-field propagation even after the application of stress modulation.

Fig. 8(k) illustrates the far-field energy distribution of the test pulse before and after stress loading, covering both the transverse target plane and the longitudinal region near focus. The comparison of the transverse focal spot energy distributions reveals that the fraction of high-energy speckles decreases significantly after the introduction of stress. In the longitudinal direction, stress induces a polarization distribution that evolves dynamically with defocus distance and leads to more pronounced fluctuations in the longitudinal energy distribution compared to the stress-free case. This modulation characteristic is more conducive to suppressing LPIs during pulse irradiation on the target.

To evaluate the actual modulation effect of edge pressure on large-aperture laser beams, an offline diagnostic system was developed to enable synchronous real-time measurements of both near-field and far-field characteristics under stress loading. As illustrated in Fig. 9(a), the measurement setup is configured as a beam expansion system with a total optical path length of approximately 28 m. The input probe beam has the diameter of 10 mm and is converted into a pure P-polarized state after passing through the polarizer. Subsequently, the beam is expanded to 52 times its initial diameter via two lens assemblies (f = 250 mm, 13 m; clear apertures = 25.4 mm, 430 mm). This configuration generates a collimated large-aperture beam, ensuring that its optical field distribution fully covers the clear aperture of the downstream components. Sufficient space is reserved between the two large-aperture lenses to accommodate optical elements such as the CPP and VW. Additionally, a polarization imaging camera is integrated into this section to precisely measure the polarization state at arbitrary positions within the clear aperture. After passing through the rear large-aperture lens, the beam is demagnified and focused onto the focal plane. In front of the target area, the switchable attenuator and polarizer are deployed, enabling the CCD camera to precisely characterize the far-field focal spots corresponding to different polarization states. To acquire the complete near-field distribution, the CCD camera located at the focal plane is removed to clear the optical path. The beam subsequently diverges from the focal plane and is collimated by a small-aperture lens (f = 150 mm, clear aperture = 25.4 mm), thereby reconstructing the scaled consistent near-field distribution. By employing another CCD camera positioned behind this lens, precise measurements of the near-field polarization component distributions can be performed. To match the spectral response of the cameras and facilitate system alignment, a standard 532 nm laser is adopted as the light source, coinciding with the second-harmonic wavelength of high-power laser systems. Furthermore, the large-aperture lenses and CPP optic in the setup are identical to those in the high-power laser facility, ensuring high consistency between offline measurements and actual online operational conditions.

To realize the edge pressure and stress tensor field distribution specified by the optimization results, a composite

Downloaded from https://www.cambridge.org/core. 11 Nov 2026 at 09:59:05, subject to the Cambridge Core terms of use.

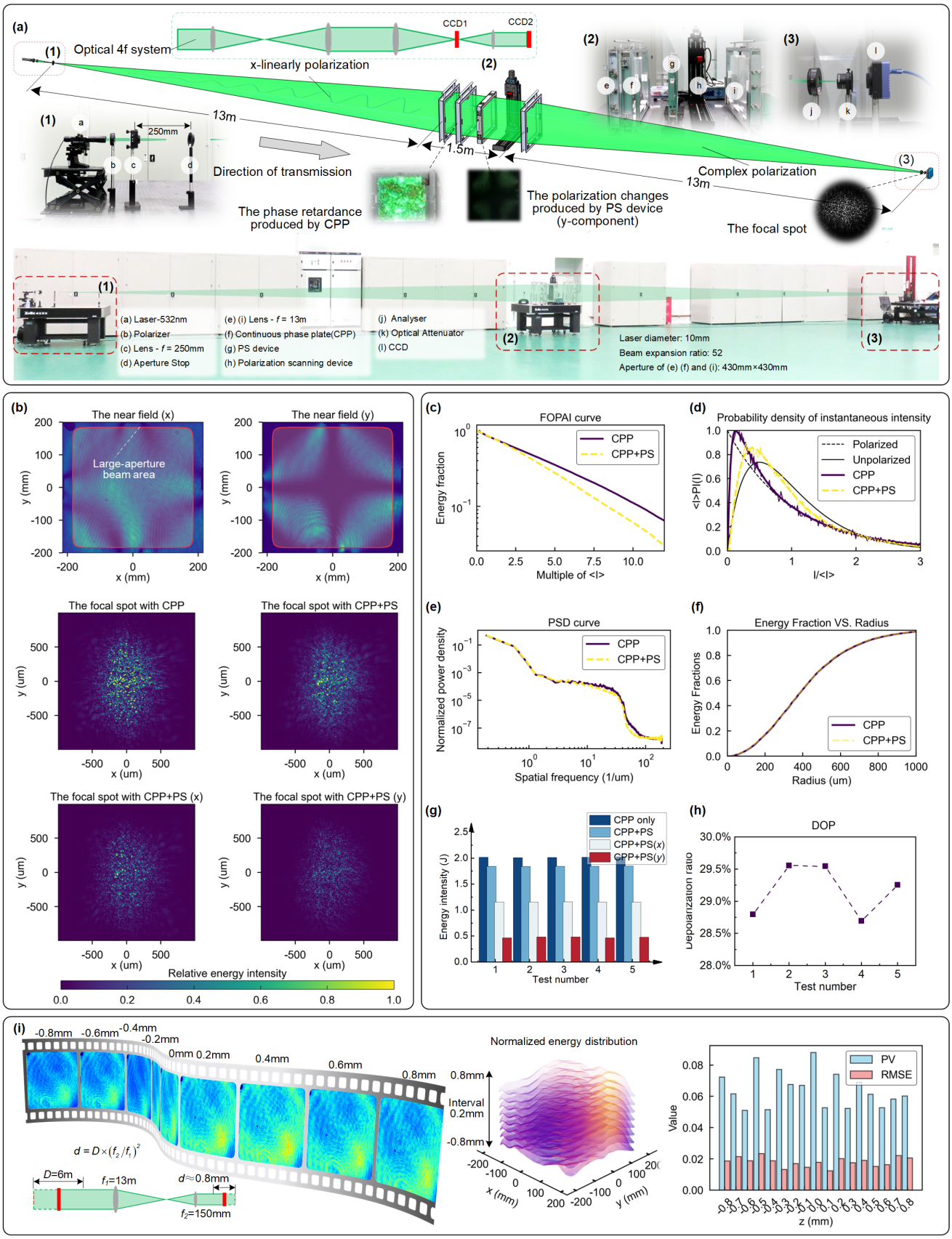


Figure 9. **(a)** Configuration of the offline measurement setup. **(b)** Near-field and far-field energy distributions. **(c)** FOPAI curves of the focal spot energy distribution. **(d)** Instantaneous intensity probability density curves of the focal spot energy distribution. **(e)** Power density spectrum of the focal spot energy distribution. **(f)** Encircled energy curves of the focal spot energy distribution. **(g)** Energy statistics of different focal spots. **(h)** The beam depolarization ratio under repeated measurements. **(i)** Near-field energy distributions during beam propagation

Downloaded from https://www.cambridge.org/core. 11 Nov 2026 at 09:59:05, subject to the Cambridge Core terms of use.

structure consisting of a 0.25 mm-thick copper pad and a 0.75 mm-thick F246 rubber pad was employed to match the σ_{gauss} parameter. Meanwhile, preloads of 2.8×10^3 N at the center and 6.22×10^3 N at two symmetric eccentric positions were applied to achieve the required pressure amplitudes.

Upon completion of the preloading process, the optical modulation effects induced by the internal stress tensor field within the VW were evaluated. As shown in Fig. 9(b), the near-field and far-field energy distributions of the probe beam after stress loading are presented. In the near-field energy distribution, the internal stress tensor field induced by edge pressure successfully reproduced the simulated polarization distribution transformation. However, the increase in the measurement wavelength relative to the simulation wavelength reduces the phase retardation under identical stress levels, resulting in a lower proportion of converted S-polarized components compared to the simulation results, which is consistent with the theoretical derivation in Eq. (6). For the far-field distribution, the total energy distributions were measured for configurations with CPP only and with CPP+PS. The energy distributions of the P- and S-polarization components were also measured for the CPP+PS configuration. Since the CPP optic in the measurement setup corresponds to the 45° incident sub-beam of the high-power laser facility, the induced phase modulation results in an elliptical envelope of the focal spot at the target plane, ensuring a circular energy map on the pellet. It can be observed that, compared with the phase modulation induced by CPP alone, the combination of stress-induced PS and CPP significantly reduces the fraction of high-power-density speckles within the focal spot, while resulting in finer and denser speckle patterns. Fig. 9(c) shows the Fraction of Power Above Intensity (FOPAI) curves, representing the power fraction exceeding multiples of the average intensity within the focal spot. Upon imposing the stress tensor field, the slope of the FOPAI curve decreases markedly, indicating effective suppression of high-power-density speckles within the focal spot. The instantaneous intensity probability density curves in Fig. 9(d) characterize the statistical properties of intensity fluctuations within the focal spot speckle field. For the polarized thermal light (degree of polarization $P = 1$), the ratio of the standard deviation to the mean of the instantaneous intensity is unity. For the completely unpolarized thermal light ($P = 0$), this ratio decreases to $1/\sqrt{2}$, which arises from the statistical optics of the complete incoherent superposition of speckle fields. Fig. 9(d) demonstrates that imposing the stress tensor field causes a sharp decrease in the instantaneous intensity probability density for the 532 nm beam, indicating a substantial degree of incoherent superposition between the two polarization components. According to statistical optics, this effect becomes more pronounced at shorter wavelengths. Fig. 9(e) compares the transverse power spectral density (PSD) of the focal spot before and after the introduction of stress. It can be observed that imposing the stress tensor field shifts the PSD curve toward lower spatial frequencies, indicating that the stress effectively suppresses the high-frequency speckle components associated with rapid energy fluctuations within the focal spot. Fig. 9(f) evaluates the encircled energy distributions of the focal spot before and after imposing the stress tensor field. It can be observed that the enclosed energy fractions remain nearly identical across different radii, indicating that the stress-induced transmitted wavefront distortion does not cause a significant expansion of the focal spot radius. Figs. 9(g) and 9(h) present the statistical results of beam energy under multiple repeated experimental conditions. With the combined CPP and stress-inducing PS elements, reflections from the front and rear surfaces of the added VW result in partial beam energy loss. Under the combined action of the stress tensor field and multiple optics, the beam forms the focal spot with a complex polarization distribution. Using an analyzer, we quantitatively measured the energy fractions of the residual P-polarized component and the converted S-polarized component. The results show that at 532 nm, the stress tensor field induces conversion of approximately 29% of the beam energy to S-polarization; whereas at 351 nm, this proportion can increase to about 41%.

To analyze whether the stress-induced beam would generate unacceptable spatial energy modulation during subsequent propagation, we evaluated the near-field energy distribution over a propagation distance of 6 m. As shown in Fig. 9(i), in the 4f system, the propagation distance D of the large-aperture beam and the propagation distance d of the downscaled small-aperture beam satisfy the relation $d = D \times (f_2/f_1)$. Based on this, the CCD is required to shift by 0.8 mm along the optical path to characterize the evolution of the energy intensity of the large-aperture beam over a near-field propagation range of 6 m. Taking the optical field image plane at the rear surface of the VW as the zero reference, we employed a micrometer translation stage to move the camera within a range of ±0.8 mm, and recording the field distributions at intervals of 0.1 mm. We observed that the overall morphology of the near-field energy distribution remained consistent across different longitudinal positions. Concurrently, we normalized each recorded frame and analyzed their PV and RMS values relative to the global average distribution. The results show that the RMS values remained stable at approximately 2%, demonstrating that the stress tensor field does not induce significant energy modulation during propagation.

3.3. Integrated Experimental Diagnosis

To further investigate the polarization smoothing performance of the proposed scheme in practical high-power laser systems, the online experiment was conducted on the Integrated Experimental Precision Diagnostic System (PDS) of a high-power laser driver. As shown in Fig. 10(a), The VW subjected the designed stress distribution was installed at the reserved interface between the DKDP third harmonic generation crystal (THG) and the WFL, so that the stress

Downloaded from https://www.cambridge.org/core. 11 Nov 2026 at 09:59:05, subject to the Cambridge Core terms of use.

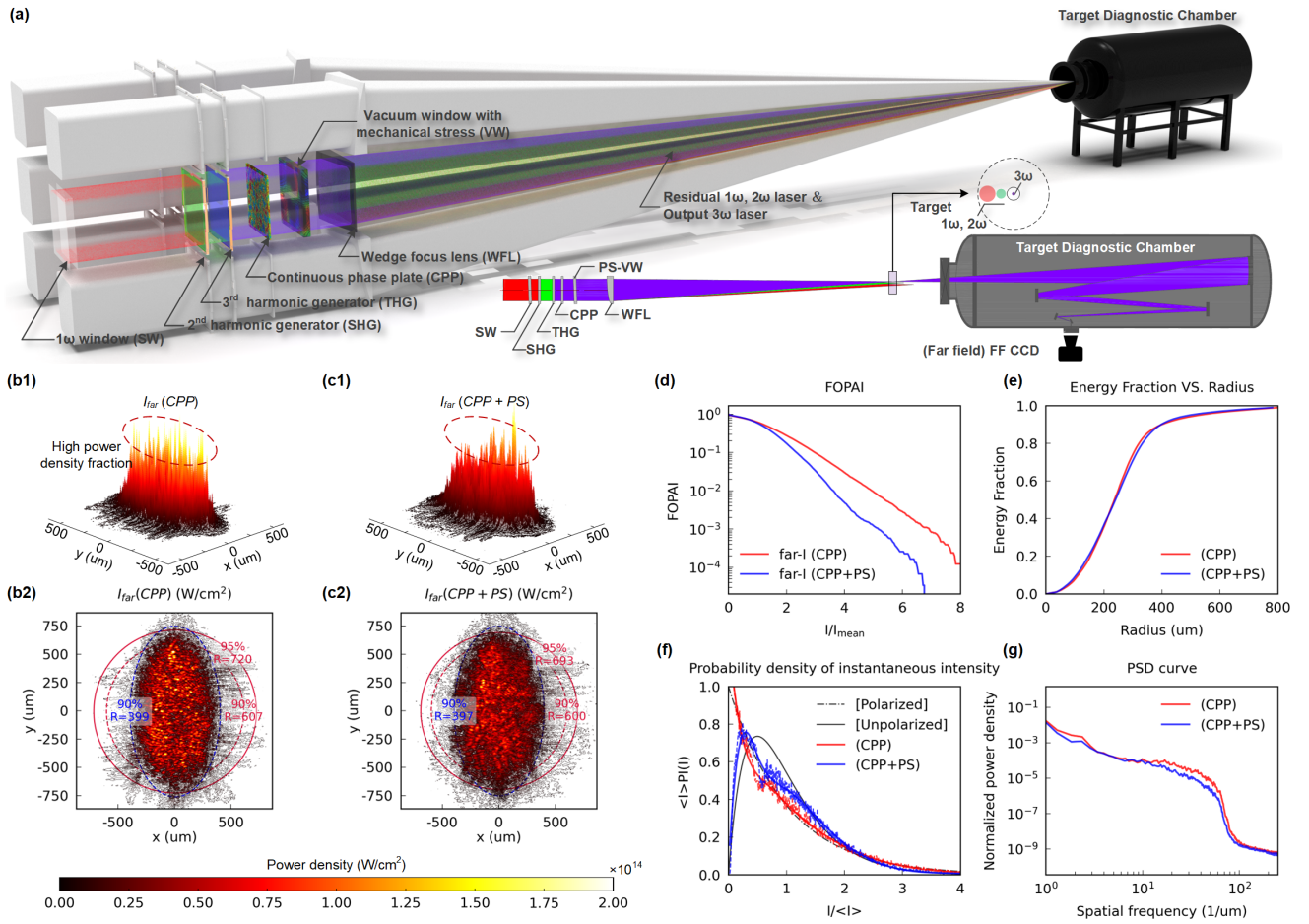


Figure 10. Online validation results of the stress modulated polarization smoothing scheme. **(a)** Schematic of the Integrated Experimental Precision Diagnostic System (PDS) of a high-power laser facility and the location of the stress optic. **(b)** Far-field (3ω, 351 nm) speckle energy distribution with only the CPP optic installed. **(c)** Far-field (3ω, 351 nm) speckle energy distribution with both the CPP optic and the stress induced PS optic installed. The measurements in (b) and (c) were both carried out along the same diagnostic beamline shown in (a), and the same CPP optic was used in both measurements. **(d)** FOPAI curves of the focal spot. **(e)** Encircled energy curves of the focal spot energy distribution. **(f)** Energy statistics of different focal spots. **(g)** Power density spectrum of the focal spot energy distribution.

modulation acted directly on the 3ω laser beam (351 nm). After polarization modulation, the 3ω beam, together with the residual 1ω beam (1053 nm) and 2ω beam (527.5 nm) after harmonic conversion, was focused toward the target region through the WFL. Because the beams with different wavelengths are focused along different directions, the 1ω and 2ω beams were spatially separated from the 3ω beam in the target region and were removed by physical isolation. After passing through the focus, the 3ω beam entered the target diagnostic chamber (TDC), where its far field focal spot energy distribution was recorded by a CCD camera after reflection and attenuation.

Figures 10(b) and 10(c) show the far field speckle energy distributions measured by the CCD in the TDC during two main shots, with only the CPP optic installed (CPP shot) and with both the CPP and the stress PS optics installed (CPP+PS shot), respectively. Both main shots were performed using the same diagnostic beamline in the PDS shown in Fig. 10(a). The same CPP and other optics were used in both shots, with identical installation positions and system parameters, so as to minimize the influence of other factors on the experimental results. The output energies of the two main shots were of the same order of magnitude but were not exactly identical, with 850.7 J for the CPP shot and 817.1 J for the CPP+PS shot. Therefore, the two shots were normalized to the same reference energy during data processing to avoid the influence of the energy difference on the speckle statistics.

From the 3D far field speckle energy distributions shown in Figs. 10(b1) and 10(c1), the high-power density peaks in the original speckle field are clearly reduced under the designed stress field, and the fraction of high-power density speckles is significantly decreased. This indicates that stress induced polarization modulation can effectively suppress local high energy density fluctuations in the target region. Figures 10(b2) and 10(c2) show the energy concentration of the CPP shot and CPP+PS shot. Circular and elliptical regions with an

Downloaded from https://www.cambridge.org/core. 11 Nov 2026 at 09:59:05, subject to the Cambridge Core terms of use.

aspect ratio of 1700:900 were used to calculate the encircled energy of the speckle field, where the aspect ratio of the ellipse corresponds to the designed focal spot size of the CPP used in the experiment. The focal spot sizes of the two shots remained almost unchanged (for the circular region: $R_{\text{CPP shot}}$ = 607 um, $R_{\text{CPP+PS shot}}$ = 600 um, radius change = −1.17%; for the elliptical region, with the semi minor axis defined as the equivalent radius R: $R_{\text{CPP shot}}$ = 399 um, $R_{\text{CPP+PS shot}}$ = 397 um, radius change = −0.5%). On this basis, the RMS of the speckle field within the 90% elliptical encircled energy region was further calculated, and the relative contrast before and after polarization smoothing was compared. The results show that the RMS contrast of the CPP+PS shot is reduced to approximately 0.776 times that of the CPP shot, which is consistent with the expected polarization smoothing performance of the designed stress field at 351 nm. As shown in Fig. 10(d), compared with the 532 nm offline experimental results, the FOPAI curve obtained in the 351 nm integrated diagnostic experiment shows a more pronounced decrease, indicating stronger suppression of high-power density speckles at the design wavelength. Figure 10(e) shows the encircled energy curves with varying elliptical radius. The two curves show good agreement overall and almost overlap after the encircled energy reaches approximately 90%, further indicating that the spatial separation introduced by the stress induced wavefront gradient remains on the scale of the speckle coherence length, thereby avoiding a noticeable increase in the focal spot radius while maintaining the energy concentration. In addition, as shown in Fig. 10(f), the peak of the instantaneous intensity probability density in the diagnostic experiment is further reduced, which is consistent with the decrease in the relative RMS contrast. The PSD results in Fig. 10(g) show that some high spatial frequency components are suppressed after polarization smoothing, indicating that the spatial separation and incoherent superposition of the orthogonal P and S components can effectively reduce local intensity fluctuations in the speckle field.

4. Conclusion

This study proposes a gradient-descent-based BP optimization strategy for assembly preload in stress-induced polarization smoothing of the high-power laser facility. Employing the VW as the functional stress carrier, a coupled mechanical-optical model was established to quantitatively correlate the internal stress tensor field distribution with the optical properties of the material. Leveraging the finite element method and the linear superposition principle of elasticity, we achieved a discrete solution for the stress tensor field under arbitrary symmetric edge pressures. Furthermore, we developed a theoretical propagation model covering large-aperture beams transmitting through multiple optical components and free space, and based on which we constructed a forward simulation algorithm for terminal optics sub-beams incorporating stress effects.

Based on the terminal optics sub-beam forward simulation algorithm, we constructed a boundary pressure optimization framework featuring backpropagation capabilities. Through quantitative analysis based on the mechanical clamping configuration, we clarified the mapping relationship between boundary pressure and preload force, achieving parameter reduction and specification from mechanical boundary constraints to preload implementation. We integrated the mechanical coupling mechanism between boundary constraints and preload forces into the optimization framework, establishing an information transfer and feedback link from mechanical preload to the optical far field. Using a flat-top spot as the target far-field energy distribution, we optimized the preload parameters and determined the required amplitude and location of the preload force for mechanical clamping. Based on the optimized preload parameters, we simulated the optical modulation effects of the stress tensor field during the propagation of the large-aperture beam. The results indicate that this stress field significantly suppresses the fraction of high-power-density speckles in the target area and intensifies energy fluctuations along the propagation direction near the focal region, which positively contributes to the mitigation of LPIs without inducing adverse intensity modulation in the near field.

To evaluate the actual optical modulation effects induced by mechanical preload, we established a metrology system for characterizing the field modulation of the large-aperture beam and conducted experiments to measure the optical modulation introduced by the stress tensor field. Experimental results show that at the test wavelength of 532 nm, approximately 29% of the incident P-polarized energy is converted to S-polarization, whereas this conversion efficiency reaches 41% at the operating wavelength of 351 nm. Furthermore, the stress tensor field effectively suppresses high-power-density speckles, reduces temporal intensity fluctuations, optimizes the power spectral density of the focal spot, and introduces no significant wavefront aberrations or near-field modulation. To verify the actual performance of the proposed scheme at the design wavelength, an online experiment was performed at 351 nm on the Precision Diagnostic System (PDS) of a high-power laser facility. The measured relative RMS contrast of the focal spot was reduced to approximately 0.776 of that obtained with the CPP alone, which agrees well with the numerical prediction of approximately 0.77 at 351 nm. Meanwhile, compared with the 532 nm offline experiment, the FOPAI curve at 351 nm showed a greater reduction, while the focal spot size and energy concentration remained nearly unchanged. The combined results from the 532 nm offline experiment and the 351 nm online experiment verify that the proposed stress induced polarization smoothing method can maintain beam quality while providing stable speckle suppression in the target region under practical high power laser conditions.

This method provides a controllable solution for polarization smoothing in high-power laser drivers. The future work

Downloaded from https://www.cambridge.org/core. 11 Nov 2026 at 09:59:05, subject to the Cambridge Core terms of use.

will focus on cooperative strategies for stress-induced polarization smoothing among multiple sub-beams within the bundle, aiming to achieve adaptive preload feedback and multi-actuator coordinated control targeting energy uniformity on the target plane during multi-beam operations, thereby further enhancing the adaptability and long-term stability of the system.

Acknowledgement

This work was supported in part by the National Natural Science Foundation of China under Grant (No.52375475, No.12405280 and No.12204443) and the Youth Talent Growth Foundation of Laser Fusion Research Center, CAEP (NO. RCFPD6-2022-3). The authors appreciate the contributions and efforts of engineers in Research Center of Laser Fusion, China Academy of Engineering Physics.

References

1. John D Lindl, Peter Amendt, Richard L Berger, S Gail Glendinning, Siegfried H Glenzer, Steven W Haan, Robert L Kauffman, Otto L Landen, and Laurence J Suter. The physics basis for ignition using indirect-drive targets on the national ignition facility. *Physics of plasmas*, 11(2):339–491, 2004.
2. Stefano Atzeni and Jürgen Meyer-ter Vehn. *The Physics of Inertial Fusion: BeamPlasma Interaction, Hydrodynamics, Hot Dense Matter*. Number 125. Oxford University Press, 2004.
3. DH Froula, L Divol, RA London, RL Berger, T Döppner, NB Meezan, J Ralph, JS Ross, LJ Suter, and SH Glenzer. Experimental basis for laser-plasma interactions in ignition hohlraums at the national ignition facility. *Physics of Plasmas*, 17(5), 2010.
4. DE Hinkel, MD Rosen, EA Williams, AB Langdon, CH Still, DA Callahan, JD Moody, PA Michel, RPJ Town, RA London, et al. Stimulated raman scatter analyses of experiments conducted at the national ignition facility. *Physics of Plasmas*, 18(5), 2011.
5. Wang Qiang, Liu Zhanjun, Zheng Chunyang, Li Xin, Cao Lihua, Hao Liang, and Cai Hongbo. Analysis of stimulated brillouin scattering in icf hohlraum excited by multi-color incoherent lights. *High Power Laser and Particle Beams*, 33(10):102001–1, 2021.
6. L Hao, J Li, WD Liu, R Yan, and C Ren. Simulation of stimulated brillouin scattering and stimulated raman scattering in shock ignition. *Physics of Plasmas*, 23(4), 2016.
7. James F Drake, Predhiman K Kaw, Yee-Chun Lee, G Schmid, Chuan S Liu, and Marshall N Rosenbluth. Parametric instabilities of electromagnetic waves in plasmas. *Physics of Fluids*, 17(4):778–785, 1974.
8. DW Forslund, JM Kindel, and EL Lindman. Theory of stimulated scattering processes in laser-irradiated plasmas. *The Physics of Fluids*, 18(8):1002–1016, 1975.
9. Mary L Spaeth, KR Manes, DH Kalantar, PE Miller, JE Heebner, ES Bliss, DR Spec, TG Parham, PK Whitman, PJ Wegner, et al. Description of the nif laser. *Fusion Science and Technology*, 69(1):25–145, 2016.
10. JL Miquel, C Lion, and P Vivini. The laser mega-joule: Lmj & petal status and program overview. In *Journal of Physics: Conference Series*, volume 688, page 012067. IOP Publishing, 2016.
11. Jerome Neauport, Jean Philippe Airiau, Nicolas Beck, Nicolas Belon, Edouard Bordenave, Stéphane Bouillet, Margaux Chanal, Céline Chappuis, Hervé Coic, Roger Courchinoux, et al. Laser megajoule performance status. *Applied Optics*, 63(16):4447–4464, 2024.
12. Wanguo Zheng, Xiaofeng Wei, Qihua Zhu, Feng Jing, Dongxia Hu, Xiaodong Yuan, Wanjun Dai, Wei Zhou, Fang Wang, Dangpeng Xu, et al. Laser performance upgrade for precise icf experiment in sg-iii laser facility. *Matter and Radiation at Extremes*, 2(5):243–255, 2017.
13. Dong Yang, Zhichao Li, Sanwei Li, Liang Hao, Xin Li, Liang Guo, Shiyang Zou, Xiaohua Jiang, Xiaoshi Peng, Tao Xu, et al. Laser plasma instability in indirect-drive inertial confinement fusion. *Scientia Sinica Physica, Mechanica & Astronomica*, 48(6):065203, 2018.
14. D Pesme, S Hüller, J Myatt, C Riconda, A Maximov, VT Tikhonchuk, C Labaune, J Fuchs, S Depierreux, and HA Baldis. Laser–plasma interaction studies in the context of megajoule lasers for inertial fusion. *Plasma physics and controlled fusion*, 44(12B):B53–B67, 2002.
15. E Moses. Multi-megajoule nif: Ushering in a new era in high energy density science. In *High-Power Laser Ablation VII*, volume 7005, pages 125–135. SPIE, 2008.
16. Yoshiaki Kato, K Mima, N Miyanaga, S Arinaga, Y Kitagawa, M Nakatsuka, Yamanaka, and C. Random phasing of high-power lasers for uniform target acceleration and plasma-instability suppression. *Physical Review Letters*, 53(11):1057, 1984.
17. SN Dixit, MD Feit, MD Perry, and HT Powell. Designing fully continuous phase screens for tailoring focal-plane irradiance profiles. *Optics Letters*, 21(21):1715–1717, 1996.
18. John A Marozas. Fourier transform–based continuous phase-plate design technique: a high-pass phase-plate design as an application for omega and the national ignition facility. *Journal of the Optical Society of America A*, 24(1):74–83, 2006.
19. Li Ping, Ma Chi, Su Jingqin, Cheng Wenyong, Liu Lanqin, Wang Wenyi, Mo Lei, and Zhou Lidan. Design of continuous phase plates for controlling spatial spectrum of focal spot. *High Power Laser and Particle Beams*, 20, 2008.
20. RS Craxton, KS Anderson, TR Boehly, VN Goncharov, DR Harding, JP Knauer, RL McCrory, PW McKenty,

Downloaded from https://www.cambridge.org/core. 11 Nov 2026 at 09:59:05, subject to the Cambridge Core terms of use.

DD Meyerhofer, JF Myatt, et al. Direct-drive inertial confinement fusion: A review. *Physics of Plasmas*, 22(11), 2015.

21. EM Campbell, VN Goncharov, TC Sangster, SP Regan, PB Radha, R Betti, JF Myatt, DH Froula, MJ Rosenberg, IV Igumenshchev, et al. Laser-direct-drive program: Promise, challenge, and path forward. *Matter and Radiation at Extremes*, 2(2):37–54, 2017.
22. RH Lehmberg and SP Obenschain. Use of induced spatial incoherence for uniform illumination of laser fusion targets. *Optics Communications*, 46(1):27–31, 1983.
23. RH Lehmberg, AJ Schmitt, and SE Bodner. Theory of induced spatial incoherence. *Journal of applied physics*, 62(7):2680–2701, 1987.
24. S Skupsky, RW Short, T Kessler, RS Craxton, S Letzring, and JM Soures. Improved laser-beam uniformity using the angular dispersion of frequency-modulated light. *Journal of Applied Physics*, 66(8):3456–3462, 1989.
25. Joshua E Rothenberg. Polarization beam smoothing for inertial confinement fusion. *Journal of Applied Physics*, 87(8):3654–3662, 2000.
26. Pierre Michel. Optical smoothing of high-power lasers and implications for laser–plasma instabilities. In *Introduction to Laser-Plasma Interactions*, pages 315–369. Springer, 2023.
27. Pierre Michel, Laurent Divol, David Turnbull, and John D Moody. Dynamic control of the polarization of intense laser beams via optical wave mixing in plasmas. *Physical review letters*, 113(20):205001, 2014.
28. K Tsubakimoto, M Nakatsuka, H Nakano, T Kanabe, T Jitsuno, and S Nakai. Suppression of interference speckles produced by a random phase plate, using a polarization control plate. *Optics communications*, 91(1-2):9–12, 1992.
29. Yinrui Zhang, Yuan Huang, Zheqiang Zhong, and Bin Zhang. Analysis of the smoothing performance of a rapid polarization rotation smoothing scheme. *Applied Optics*, 59(15):4624–4633, 2020.
30. Yanghui Tang, Shenlei Zhou, Shouying Xu, and Cheng Liu. Focal spot polarization distribution under polarization smoothing. *High Power Laser Science and Engineering*, 13:e21, 2025.
31. David H Munro, Shamasundar N Dixit, A Bruce Langdon, and John R Murray. Polarization smoothing in a convergent beam. *Applied optics*, 43(36):6639–6647, 2004.
32. SN Dixit, D Munro, JR Murray, M Nostrand, PJ Wegner, D Froula, CA Haynam, and BJ MacGowan. Polarization smoothing on the national ignition facility. In *Journal de Physique IV (Proceedings)*, volume 133, pages 717–720. EDP sciences, 2006.
33. TR Boehly, VA Smalyuk, DD Meyerhofer, JP Knauer, DK Bradley, RS Craxton, MJ Guardalben, S Skupsky, and TJ Kessler. Reduction of laser imprinting using polarization smoothing on a solid-state fusion laser. *Journal of applied physics*, 85(7), 1999.
34. Xiaoxia Huang, Huaiting Jia, Wei Zhou, Fan Zhang, Huaiwen Guo, and Xuewei Deng. Experimental demonstration of polarization smoothing in a convergent beam. *Applied Optics*, 54(33):9786–9790, 2015.
35. Hu Huang, Tanya Z Kosc, Terrance J Kessler, and Stavros G Demos. Modeling of transverse stimulated raman scattering in kdp/dkdp in large-aperture plates suitable for polarization control. *High Power Laser Science and Engineering*, 11:e54, 2023.
36. Yajing Guo, Shunxing Tang, Hongchao Hui, Yuyu Wang, Qing Tang, Baoqiang Zhu, and Zunqi Lin. Transverse stimulated raman scattering gain coefficient measurement in kdp crystal. In *Pacific Rim Laser Damage 2013: Optical Materials for High Power Lasers*, volume 8786, pages 131–138. SPIE, 2013.
37. Alexis K Spilman and Thomas G Brown. Stress birefringent, space-variant wave plates for vortex illumination. *Applied optics*, 46(1):61–66, 2006.
38. Tiecheng Liu, Jingpei Hu, Linglin Zhu, Ruyi Zhou, Chong Zhang, Liyuan Gu, Xiaodong Sun, Jianfei Yu, Aijun Zeng, and Huijie Huang. Mechanical stress birefringence of optical plates. *Applied Optics*, 59(24):7371–7375, 2020.
39. Alexis K Spilman and Thomas G Brown. Stress-induced focal splitting. *Optics Express*, 15(13):8411–8421, 2007.
40. Zongyong Pan and Xiaomin Pan. Deep learning and adjoint method accelerated inverse design in photonics: a review. In *Photonics*, volume 10, page 852. MDPI, 2023.
41. Qingming Liao, Haoqiang Wang, Zexin Feng, Mengmeng Li, Yi Luo, and Xianglong Mao. Differentiable design of freeform diffractive optical elements for beam shaping by representing phase distribution using multi-level b-splines. *Optics Express*, 32(23):41041–41056, 2024.

Downloaded from https://www.cambridge.org/core. 11 Nov 2026 at 09:59:05, subject to the Cambridge Core terms of use.